Fişa suspiciunii de plagiat / Sheet of plagiarism's suspicion	Indexat la: 22/06

Opera suspicionată (OS) Suspicious work	Opera autentică (OA) Authentic work

OS	Raveica, I.C., Schnakovszky, C., „Studies concerning the contact between two asperities in deforming and milling process", *Annals of the Oradea University. Fascicle of Management and Technological Engineering, Volume VII (XVII), p.1746-1752, 2008.*
OA	Boucly, V., Nélias, D., Green, I., „Modeling of the Rolling and Sliding Contact Between Two Asperities", *Journal of Tribology*, Vol. 129, p.235-245, April 2007.

Incidența minimă a suspiciunii / Minimum incidence of suspicion	
p.1746:07 – p.1746:14	p.235:04 – p.235:07; p.235:12 – p.235:17
p.1746:25 – p.1747:09	p.235:29s – p.235:43s
p.1747:10 – p.1747:11	p.235:07d – p.235:09d
p.1747:14 – p.1747:18	p.235:19d – p.235:24d
p.1747:19 – p.1747:24	p.236:07s – p.236:14s
p.1747:26 – p.1748:03	p.236:16s – p.236:50s
p.1748:04 - p.1752:09	p.237:29d - p.240:14s
p.1753:09 – p.1753:25	p.244:05s – p.244:27s

Modeling of the Rolling and Sliding Contact Between Two Asperities

Vincent Boucly

Daniel Nélias

LaMCoS, UMR CNRS 5259,
INSA Lyon,
69621, Villeurbanne Cedex, France

Itzhak Green

George W. Woodruff School of Mechanical Engineering,
Georgia Institute of Technology,
Atlanta, GA 30332-0405

A semi-analytical method for the tridimensional elastic-plastic contact between two hemispherical asperities is proposed. The first part of the paper describes the algorithm used to deal with the normal contact, which can be either load-driven or displacement-driven (dd). Both formulations use the conjugate gradient method and the discrete convolution and fast Fourier transform (DC-FFT) technique. A validation of the code is made in the case of the displacement-driven formulation for an elastic-plastic body in contact with a rigid punch, simulating a nano-indentation test. Another new feature is the treatment of the contact between two elastic-plastic bodies. The model is first validated through comparison with the finite element method. The contact pressure distribution, the hydrostatic pressure and the equivalent plastic strain state below the contacting surfaces are also found to be strongly modified in comparison to the case of an elastic-plastic body in contact with a purely elastic body. The way to consider rolling and sliding motion of the contacting bodies consists of solving the elastic-plastic contact at each time step while upgrading the geometries as well as the hardening state along the moving directions. The derivations concerning the interference calculation at each step of the sliding process are then shown, and an application to the tugging between two spherical asperities in simple sliding (dd formulation) is made. The way to project the forces in the global reference is outlined, considering the macro-projection due to the angle between the plane of contact and the sliding direction, and the micro-projection due to the pile-up induced by the permanent deformation of the bodies due to their relative motion. Finally, a load ratio is introduced and results are presented in terms of forces, displacements, and energy loss in the contact. [DOI: 10.1115/1.2464137]

Keywords: contact modeling, elastic-plastic contact, SAM method, tangential and normal loading, sliding

1 Introduction

It is now well recognized that semi-analytical methods (SAMs) are efficient methods for solving contact problems. Compared to finite element (FE) analyses, SAMs show much shorter computation times, typically by several orders of magnitude. In SAM, analytical formulas are derived using Green functions, commonly called influence coefficients in the discrete form. Quantities are then obtained by numerical computing using accelerating techniques, leading to extremely short computation times. Among many numerical methods it seems that the most efficient to solve contact problem are the conjugate gradient method (CGM) first introduced by Polonsky and Keer [1], the multi-level multi-summation technique first implemented by Lubrecht and Ioannides [2], the fast Fourier transform (FFT) introduced by Ju and Farris [3] and used by Nogi and Kato for contact problems with layers [4]. The FFT technique has been further improved for discrete convolution problems (DC-FFT) [5] and combined to the CGM by Liu et al. [6]. The present paper is in the continuity of the work by Nélias and co-workers [7–13] who developed a semi-analytical method for solving contact problems with different levels of complexity ranging from elastic-plastic (EP) rolling contact simulation [7], thermal-elastic-plastic (TEP) analysis [8], normally and tangentially loaded EP contact [9] with various potential applications such as the determination of the micro-yield stress profile in a nitrided steel by nano-indentation [10], the rolling of a load on a smooth, dented, or rough surface [7,11], the simulation of fretting wear [12], and the running-in or wear of initially smooth or rough surfaces [13]. Elastic-plastic contact has been also recently studied by Wang and Keer [14] and also Popescu et al. [15,16] with a very similar method.

The first part of the paper is focused on the simulation of the normal contact, which is the first step in the modeling of asperities tugging in simple sliding motion. For that purpose the TEP contact model has been improved in two ways; (i) by driving the simulation by displacement increments instead of a load-driven (ld) formulation as used before, and (ii) the elastic-plastic behavior of each contacting body is now considered, instead of one elastic-plastic material loaded against an elastic one in previous work. It should be pointed out that the displacement-driven (dd) formulation is well adapted to the localized contact between two opposite asperities since the load distribution between asperities for real rough surfaces is not known a priori.

The way to consider rolling and sliding motion of the contacting bodies consists of solving the elastic-plastic contact at each time step while upgrading the geometries as well as the hardening state along the moving directions. An application to the tugging between two spherical asperities in simple sliding (dd formulation) is made in the second part of the paper.

Sliding contacts are present in many mechanical components. They are also observed in human joints, as pointed out by Chen et al. [17], where a 2D simulation has been performed using the finite element method (FEM). This modeling is similar to the one used by Vijaywargiya and Green [18]. The latter are the first researchers who uncoupled the effect of mechanical deformation and the effect of friction in sliding contacts. Previous researchers

Contributed by the Tribology Division of ASME for publication in the JOURNAL OF TRIBOLOGY. Manuscript received April 19, 2006; final manuscript received November 27, 2006. Review conducted by Jane Wang. Paper presented at the STLE/ASME 2006 International Joint Tribology Conference (TRIB2006), San Antonio, Texas, October 22–25, 2006.

 Copyright © 2007 by ASME

tried to model sliding contact, but they actually studied the effect of an increase in the friction coefficient on the contact between a sphere and a rigid flat [19–21] or between two spheres [22], the latter showing extremely long execution times. Nosonovsky and Adams simulated the contact between two cylinders [23] whose surface is not smooth.

The current paper focuses only on the mechanical deformation involved in sliding contact in order to uncouple the phenomenon. Compared to previous researchers' models, the proposed method can be applied either to statistical or deterministic approaches, in order to study the rolling and sliding thermal-elastic-plastic contact between real 3D rough surfaces. It is to be noted that the bodies in contact can follow any hardening law; i.e., they are not restricted to be perfectly plastic.

2 Load-Driven (ld) versus Displacement-Driven (dd) Formulations

In order to simulate the rolling/sliding contact, a ld formulation was first used by applying a normal load (vertical loading) prior to the tangential displacement of the load (rolling load). In such a formulation one may consider a frictionless contact, see, for example [7,8,11], as well as the effect of friction, which often tends to overload the near-surface area [9,13]. This formulation is well adapted when considering the whole contact between two bodies pressed against each other with a prescribed load. On the other hand, when focusing the analysis to the contact between two single asperities led on opposite surfaces that are in relative motion, it is clear that this localized interaction is more related to a rigid body displacement (interference) producing a transient normal and tangential loading when asperities collide. It should be noted that the tangential load is here defined as the force that acts opposite to the relative velocity, which is not limited to frictional effects since the contact surface is barely parallel to the relative velocity between the contacting surfaces. This is the reason a friction coefficient is purposely omitted in this study; i.e., in order to uncouple tangential effects induced by mechanical deformations, and the ones induced by friction. The mechanism at the origin of the tangential load found when two asperities tug each other is similar to the one found during ploughing when a normally loaded rigid indenter is translated on the surface of a deformable media.

A realistic application of the sliding between two asperities with a fixed value of the interference could be the sliding of a projectile between two rails in an electromagnetic launcher for example, since the projectile is sliding on two rails that are fixed in distance.

Basically the load-driven formulation shows very good results in terms of convergence rate and accuracy, but the user is forced to fix a value for the load, resulting in finding a rigid body displacement after computation. As said earlier, this is convenient for the resolution of the whole contact, but not to describe the tugging between two single asperities. Thereafter, the contact algorithm for the displacement-driven formulation is presented.

2.1 Elastic Contact Problem. The contact problem can be described by the following system of equations and inequalities

$$\sum_{(k,l)\in I_g} K_{i-k,j-l}p_{kl} = h_{ij} + \alpha \quad (i,j) \in I_c \tag{1a}$$

$$p_{ij} > 0 \quad (i,j) \in I_c \tag{1b}$$

$$\sum_{(k,l)\in I_g} K_{i-k,j-l}p_{kl} \geqslant h_{ij} + \alpha \quad (i,j) \notin I_c \tag{1c}$$

$$p_{ij} = 0 \quad (i,j) \notin I_c \tag{1d}$$

$$a_x a_y \sum_{(i,j)\in I_g} p_{ij} = P_0 \tag{1e}$$

where α is the rigid body approach (interference) between the two solids, a_x and a_y are the grid spacings in x and y directions respectively, P_0 is the total normal load, h_{ij} is the total separation between the two solids, and I_c denotes the set of all grid nodes that are in contact. In the case of the displacement-driven contact problem, the load is unknown, then Eq. (1*e*) is not to be solved any longer. Since one equation has been removed, one unknown—the interference α—should also be removed from the set of unknowns in the numerical procedure.

2.2 Solving the Elastic Contact Using CGM and DC-FFT. Hereafter the elastic contact algorithm used for the dd-formulation is presented. For a complete description of the algorithm for the ld-formulation and the assumptions, the reader may refer to [1].

At first, an initial value of the pressure must be fixed and Eqs. (1*b*), (1*d*), and (1*e*) have to be verified. In order to verify Eqs. (1*b*) and (1*d*), it is required to choose non-negative values for the discrete pressure. For Eq. (1*e*), for simplicity, each point of the surface is assigned a value of the pressure corresponding to the total load divided by the surface area; i.e., the number of grid points multiplied by the elementary surface area $dS = a_x \times a_y$. It is to be noticed, though, that the pressure distribution can be taken arbitrarily as long as it obeys Eq. (1*e*).

For the displacement-driven formulation, the load is unknown, but could be estimated at the initial state by using the Hertz theory.

Two variables are introduced, i.e., δ and G_{old}, which are initialized by setting $\delta = 0$ and $G_{\text{old}} = 1$.

The displacements u_{ij} are then computed and the iteration can start. The first step is the calculation of the gap g. For the displacement-driven formulation, the calculation of the gap g gives

$$g_{ij} = -u_{ij} - h_{ij} - \alpha \quad (i,j) \in I_g \tag{2}$$

Once g_{ij} is calculated, G is computed as follows

$$G = \sum_{(i,j)\in I_c} g_{ij}^2 \tag{3}$$

G and G_{old} are used for the calculation of the new conjugate direction t_{ij}

$$t_{ij} \leftarrow g_{ij} + \delta(G/G_{\text{old}})t_{ij} \quad (i,j) \in I_c \tag{4}$$

$$t_{ij} = 0 \quad (i,j) \notin I_c \tag{5}$$

and the value of G is stored in G_{old}

$$G_{\text{old}} = G \tag{6}$$

The inverted arrow notation used in Eq. (4), i.e., $A \leftarrow B$, means that to the quantity A is assigned the value of B.

In order to calculate the length of the step that will be made in the direction t_{ij}, r_{ij} is calculated as follows

$$r_{ij} = \sum_{(k,l)\in I_g} K_{i-k,j-l}t_{kl} \quad (i,j) \in I_g \tag{7}$$

Since Eq. (7) is a convolution product, the calculation of the r_{ij} is done using the DC-FFT method [5], the same way as the elastic displacements were calculated.

The length of the step τ can now be calculated

$$\tau = \frac{\sum_{(i,j)\in I_c} g_{ij}t_{ij}}{\sum_{(i,j)\in I_c} r_{ij}t_{ij}} \tag{8}$$

Before updating the pressure, the current pressure value is stored for the error calculation

$$p_{ij}^{\text{old}} = p_{ij} \quad (i,j) \in I_g \tag{9}$$

The new pressure distribution is then calculated using the previous calculated step and direction

$$p_{ij} \leftarrow p_{ij} - \pi t_{ij} \quad (i,j) \in I_c \tag{10}$$

After this step, Eq. (1*d*) must be verified. Then, for all the grid nodes where the pressure is found negative, a nil value is enforced

$$\text{if } p_{ij} < 0 \text{ then } p_{ij} = 0 \tag{11}$$

Denoting I_{ol} the set of nodes where there is no contact and where the surfaces overlap, i.e.

$$I_{\text{ol}} = \{(i,j) \in I_g: \quad p_{ij} = 0, g_{ij} < 0\} \tag{12}$$

then δ set equal to unity if $I_{\text{ol}} = \varnothing$. Otherwise, δ is set to zero and the pressures are corrected where the surfaces overlap

$$p_{ij} \leftarrow p_{ij} - \tau g_{ij} \quad (i,j) \in I_{\text{ol}} \tag{13}$$

Finally the error is computed as follows

$$\varepsilon = a_x a_y P^{-1} \sum_{(i,j) \in I_g} |p_{ij} - p_{ij}^{\text{old}}| \tag{14}$$

and a new iteration is performed, unless convergence is reached, i.e., $\varepsilon \leqslant \varepsilon_0$, with ε_0 the prescribed error.

2.3 Application to the Thermal-Elastic-Plastic Formulation. The elastic contact solver is one part of the thermal-elastic-plastic contact code. For a complete description of the problem, the reader is referred to both [7,8]. A return-mapping algorithm with an elastic predictor/plastic corrector scheme and a von Mises criterion has also been implemented, improving the plasticity loop, see [13]. This improvement in the numerical algorithm increases the computing speed significantly and shows a much better convergence and accuracy. The algorithm is given in details in [8].

Starting from an initial state that is the application of a load P or an interference α, any initial geometry, some plastic strains, and a hardening state, a first residual displacement is calculated, see [7] for calculation details. The plastic strain increment $\delta\varepsilon^p$ and the residual displacement increment δu^r are initially set to zero. The thermal-elastic contact is then calculated using the method proposed in Sec. 2.2 but replacing u_{ij} by the displacement calculated in Eq. (15) and replacing h_{ij} by the updated geometry calculated in Eq. (16), which takes into account the residual displacement found at the previous step of the iteration process. For a more detailed description, the reader is referred to [8]

$$u_{ij} = u_{ij}^e + u_{ij}^t \tag{15}$$

$$h_{ij} \leftarrow h_{ij} + u_{ij}^r \tag{16}$$

In Eq. (15), u_{ij} is the total displacement, u_{ij}^e the elastic displacement, and u_{ij}^t the thermally induced displacement [6,8], which is expressed by

$$u^t(A) = \int_\Omega mT(M)\varepsilon_{3kk}^*(M,A)d\Omega \tag{17}$$

with $m = \alpha_t[E/(1-2\nu)]$, α_t being the thermal expansion coefficient. A is the calculation point, M the integration point, $T(M)$ the temperature rise at point M of the volume Ω, and $\varepsilon_3^*(M,A)$ the elastic strain tensor at point M produced by a concentrated unit normal force (acting in the direction noted by subscript "3") applied at point A of the surface. In the case of frictional heating in the stationary regime, u^t can be rewritten as follows [8]

$$u^t(A) = \frac{\alpha_t(1+\nu)}{\pi} q ** \int_0^{+\infty} (G^T ** G^U) d\xi_3 \tag{18}$$

$q = Q_f p$ being the heat flux (W/m^2) applied on the surface, causing the temperature rise within the body. Q_f (m/s) is called the heat factor, and is equal to $Q_f = \beta\mu_f V$, β being the heat partition coefficient (equal to 1 if one of the two bodies is adiabatic); μ_f is the friction coefficient, and V (m/s) the sliding speed. G^T and G^U are two typical Green functions that can be found in [8].

In Eq. (16), h_{ij} is the updated geometry, and u_{ij}^r the residual displacement. From [7], the calculation of u_{ij}^r as a function of the plastic strain tensor gives

$$u_{ij}^r(A) = 2\mu \int_{\Omega_p} \varepsilon_{ij}^p(M)\varepsilon_{3ij}^*(M,A)d\Omega \tag{19}$$

A being the calculation point, M the integration point, μ a Lamé constant, Ω_p the volume where there are plastic strains, $\varepsilon^p(M)$ the total plastic strain tensor at point M of the volume, and $\varepsilon_3^*(M,A)$ the elastic strain tensor at point M produced by a concentrated unit normal force (acting in the direction noted by subscript "3") applied at point A of the surface.

The plastic strain increment $\delta\varepsilon^p$ is then computed, using a return mapping scheme, based on the Newton-Raphson method. The algorithm used is presented by Fotiu and Nemat-Nasser in [24], and applied to the current model in [13].

The next step is the calculation of the residual displacement increment [7] which is added to the initial geometry in Eq. (16) until convergence is reached. At this point, for a vertical loading, either the load P or the interference α is increased by an increment, and the iteration procedure is carried on. For rolling loading in the ld formulation, the load is kept constant whereas the hardening state and the plastic strains are updated after each increment. For rolling/sliding loading in the dd formulation, the interference, the hardening state and the plastic strains are updated before the next step of the iteration process.

2.4 Validation of the Displacement-Driven Algorithm. In the case of the contact between an elastic-plastic body and a rigid punch (nano-indentation test), the load-driven formulation has been validated with the finite element software ABAQUS, and also experimentally, see [7]. For this simulation, the elastic-plastic body is a flat made of steel used in aeronautic applications. The elastic properties of this steel are $E = 210$ GPa for the Young modulus, and $\nu = 0.3$ for Poisson ratio. The Swift law is used to describe the hardening behavior, see Eq. (20) and the chosen parameters are $B = 1240$ MPa, $C = 30$, and $n = 0.085$. It is to be noted that the equivalent plastic strain in this expression is expressed in microdef (10^{-6} def). These values are taken according to El Ghazal [25] and correspond to the experimental data presented in [7].

$$\sigma_{VM} = B(C + e^p)^n \tag{20}$$

For the rigid punch, a sphere with radius 105 μm is chosen (nano-indenter tip). The load is progressively applied until 0.650 N and then the two bodies are unloaded until the contact no longer occurs.

Figures 1 and 2 present a comparison between the load-driven and the displacement-driven formulations.

Figure 1 gives the evolution of the load versus the interference during loading and unloading. It is observed here the influence of both plasticity and conformity change due to permanent deformation of the surface, since the curves are really different for the loading and the unloading phases. Plasticity is a phenomenon that depends on the loading history.

The pressure distribution in the plane $y = 0$ (longitudinal plane) for an increasing load is given in Fig. 2. The pressure distribution is found flattened compared to the Hertz solution. This is due mostly to hardening of the elastic-plastic material, which tends to increase the contact area. There is also a little influence of the geometry change due to permanent deformation of the surface.

As it can be seen, a very good agreement is found, for a comparable time computation with for the mesh-size, $dx = 0.6$ μm, $dy = 1.2$ μm, $dz = 0.3$ μm, i.e., $31 \times 17 \times 44 = 23{,}188$ points in the

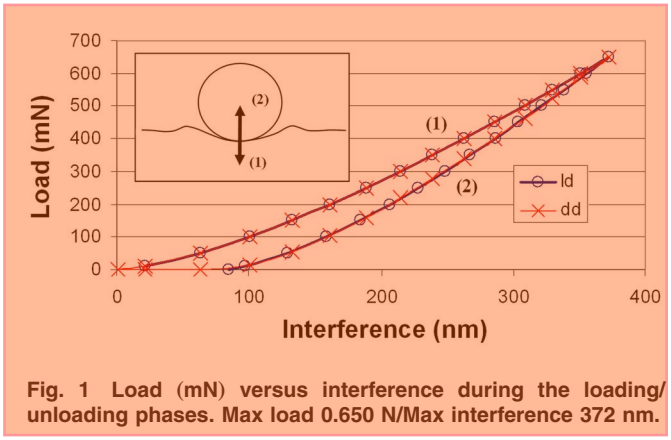

Fig. 1 Load (mN) versus interference during the loading/unloading phases. Max load 0.650 N/Max interference 372 nm.

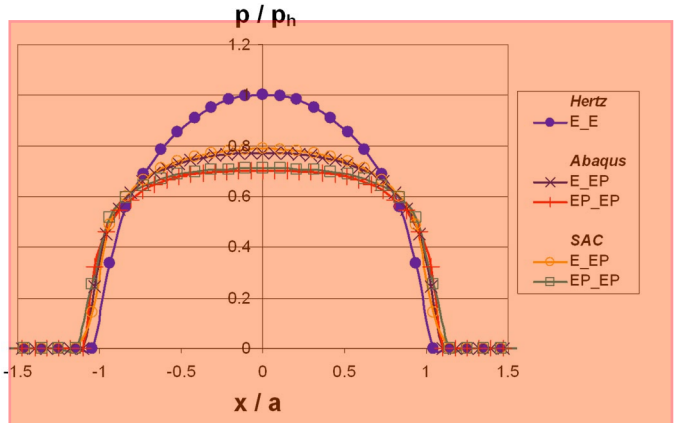

Fig. 4 Pressure distribution at the end of loading in the plane $y=0$. Load 11,179 N, i.e., $P_h=8$ GPa and Hertzian contact radius $a=817$ μm.

plastic zone and with a total of 26 time-step increments for loading/unloading (about 25 min for the whole loading/unloading process on a 1.8 GHz Pentium® M personal computer).

3 Modeling of the Contact Between Two Elastic-Plastic Bodies

This paragraph deals with the contact between two elastic-plastic bodies. The current assumptions are that the two bodies have the same initial geometry with identical elastic properties and hardening behavior. In order to validate the new proposed algorithm, a comparison with a finite element simulation is made through the normal contact between two spheres. The differences between the case of an elastic-plastic body in contact with another elastic-plastic body, and the case of an elastic-plastic body in contact with a pure elastic body will be outlined.

3.1 Improved Algorithm. The algorithm has been improved to deal with two elastic-plastic bodies in contact. The only change in the previous model is in Eq. (16). Indeed, when the initial geometry is updated, it takes into account the change in both bodies geometry at the same time since h_{ij} is actually the surface separation. At the beginning of each new increment, the pressure is calculated, and this pressure repartition is applied on both counter surfaces. The residual displacement calculated at the end of the increment is then added to the initial geometry. If one of the bodies is elastic, then the residual displacement is basically added to the initial geometry (see Fig. 3). Though, if the bodies are both elastic-plastic and have the same hardening behavior, then the surface separation in Eq. (16) becomes

$$h_{ij} \leftarrow h_{ij} + 2u^r_{ij} \tag{21}$$

because of the symmetry about the plane of contact (see Fig. 3).

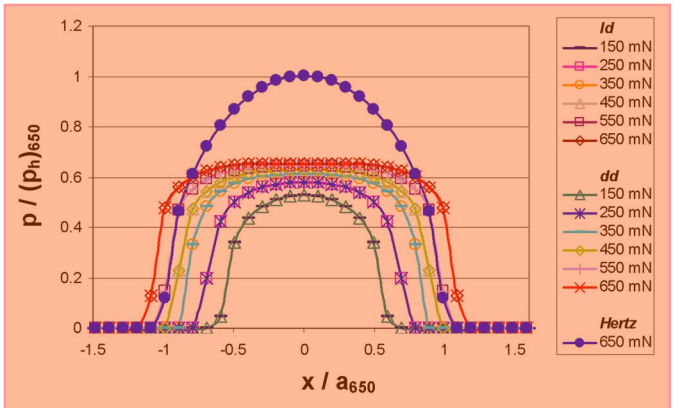

Fig. 2 Pressure distribution at the end of the loading phase, in the plane $y=0$. Load 0.650 N

3.2 Results. A simple example is proposed that corresponds to the simulation of the normal contact between two spheres of radius 15 mm. The spheres are made of AISI 52100 bearing steel, with elastic properties $E=210$ GPa for the Young modulus, and $\nu=0.3$ for the Poisson ratio. The hardening law is described by a Swift law, as in Eq. (20), with parameters $B=945$ MPa, $C=20$, and $n=0.121$. Here again, e^p is expressed in microdef.

In order to compare the results for the loaded case, Fig. 4 shows the pressure repartition at the end of the loading with a normal load of 11,179 N, corresponding to a Hertzian pressure of 8 GPa. The pressure P is normalized by the Hertzian pressure P_h, and the abscissa x by the Hertzian contact radius a. The axisymmetric FE model consists of 40,247 elements (type CAX4R) with 81,128 degrees of freedom. Two EP (Elastic-Plastic) situations are presented, the first one with only one inelastic body (E_EP), the second one when both bodies are inelastic (EP_EP, with the same hardening law). As can be seen, a very good agreement is observed between the results provided by ABAQUS and the ones from the semi-analytical code (SAC).

In order to compare the results for the unloaded case, Fig. 5 shows this time the evolution of the hydrostatic pressure as defined in Eq. (22) versus the depth, in the same conditions as before; i.e., at the end of the loading and with the same hardening

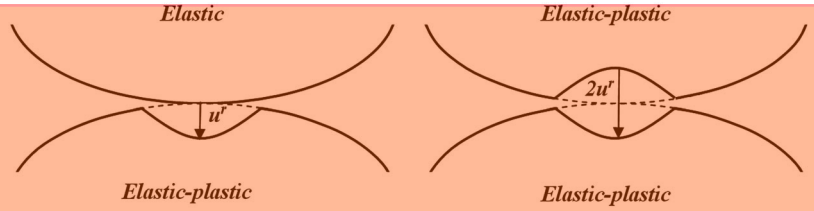

Fig. 3 Updating of the initial geometry with u^r at the beginning of a step. (*a*) Elastic body against elastic-plastic body. (*b*) Contact between 2 elastic-plastic bodies.

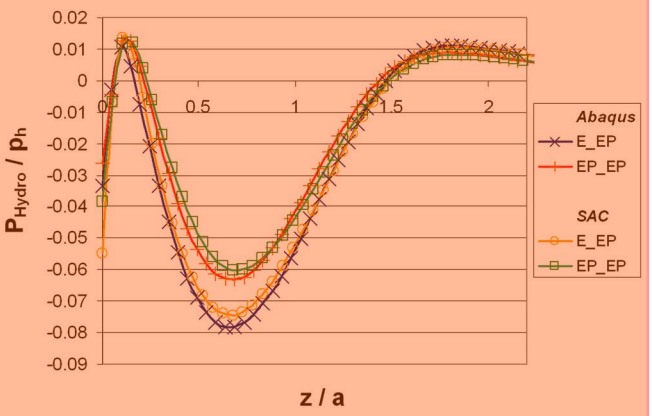

Fig. 5 Hydrostatic pressure at the end of loading at the center of the contact. Load 11,179 N, i.e., P_h=8 GPa, and Hertzian contact radius a=817 μm.

law. Again, the hydrostatic pressure is normalized by the Hertzian pressure P_h, and the depth z by the hertzian contact radius a.

$$P_{\text{hydro}} = \frac{1}{3}(\sigma_1^r + \sigma_2^r + \sigma_3^r) \tag{22}$$

with σ_1^r, σ_2^r, and σ_3^r the principal components of the residual stress tensor.

As it can be seen again, a very good agreement is observed between the results provided by Abaqus and the ones from the SAC.

One may observe two regions where the residual stress state is compressive: at the hertzian depth and at the surface, whereas two tensile regions are found: one between the surface and the Hertzian depth, but very close to the surface, and one far below the Hertzian depth.

One may also observe that the maximum compressive value is found at depth z/a=0.68; i.e., deeper than the Hertzian depth (z/a=0.48).

Almost no variation difference is found in the tensile zones, whereas an important difference in the compressive zone at the Hertzian depth is found, the minimum value being smaller when one of the bodies is considered as elastic. For more results concerning the hydrostatic pressure, and the influence of the friction coefficient on its evolution, the reader can refer to [9].

Figure 6 gives the maximum contact pressure and the corresponding maximum equivalent plastic strain versus the normal load at the center of the contact. The dash line indicates the plasticity threshold in terms of equivalent plastic strain commonly

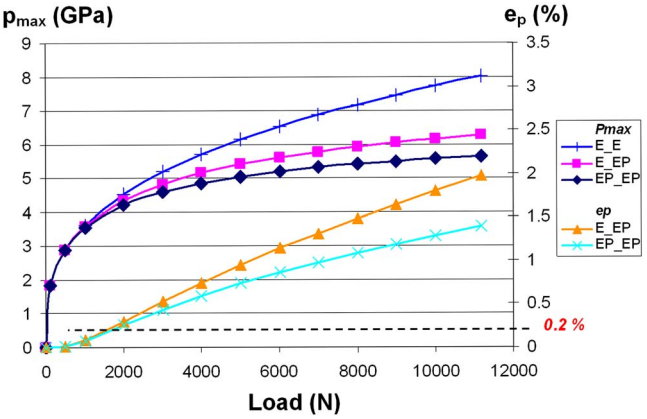

Fig. 6 Maximum contact pressure P_{max} (GPa) and equivalent plastic strain e^p (%) versus the normal load (N)

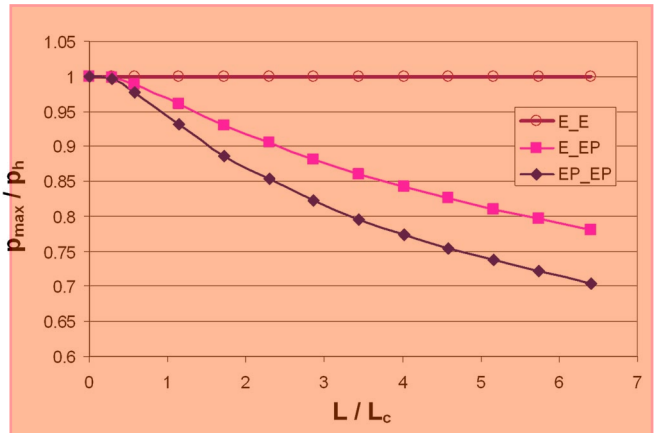

Fig. 7 Dimensionless contact pressure versus dimensionless load found at the center of the contact

used to define the yield stress, i.e., e_p=0.2%, that will be used later to define the critical load at the onset of yielding. To find the aforementioned critical value, a polynomial interpolation is used

$$P^L(x) = \sum_{j=1}^{n} P_j^L(x) \tag{23}$$

where x is equal to 0.2%, and where P_j^L are the Lagrange polynoms expressed as follows

$$P_j^L(x) = y_j \prod_{\substack{k=1 \\ k \neq j}}^{n} \frac{x - x_k}{x_j - x_k} \tag{24}$$

where x_j are the values of the equivalent plastic strains, and y_j the values of the loads.

One obtains then for the critical loads, L_c=1649 N for the case of the contact between an elastic and an elastic-plastic bodies, and L_c=1743 N for the case of the contact between two elastic-plastic bodies. The latter value will be used in what follows to present now the same results in a dimensionless form, see Fig. 7 the maximum contact pressure P_{max} being normalized by the Hertz pressure P_h and the normal load L by the critical load L_c =1743 N. An increasing difference between the two curves with increasing load can be seen. As in Fig. 6 one may also observed a pronounced reduction of the maximum contact pressure when considering two EP bodies compared to a purely elastic one against an EP one, up to 11% at the highest load (see Fig. 8). Another interesting trend in Fig. 7 is the discrepancy between the EP response compared to the Hertz solution, at the critical load; i.e., L/L_c=1. Whereas the analysis remains within the classical

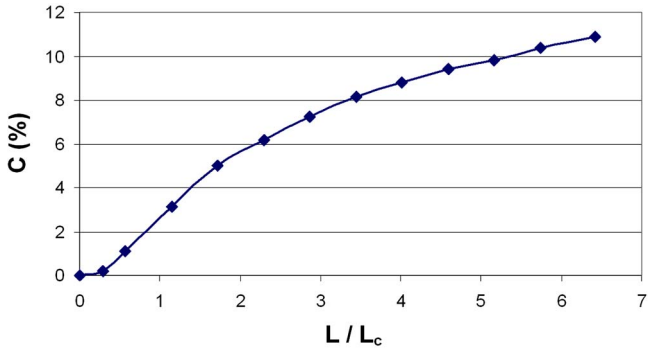

Fig. 8 Difference between the maximum contact pressures obtained assuming an E_EP and EP_EP behavior versus the dimensionless load L/L_c

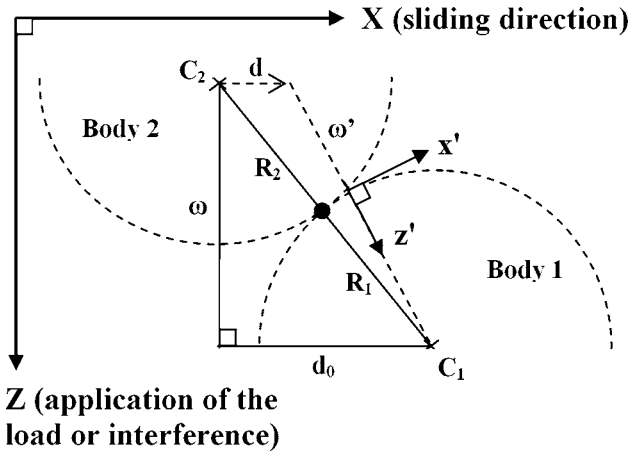

Fig. 9 Schematic view of the tugging between two interfering asperities in rolling/sliding

assumption of elastic behavior, since the plastic strain e^p does not exceed 0.2%, it appears that the real contact pressure is 5% lower than the Hertz solution when considering two EP bodies. Note that the difference between the E_EP and the EP_EP solutions is given in Fig. 8 in terms of percentage as defined by Eq. (25)

$$C(\%) = \frac{|P_{\max}^{\text{E_EP}} - P_{\max}^{\text{EP_EP}}|}{P_{\max}^{\text{EP_EP}}} 100 \tag{25}$$

From Fig. 8 it can be concluded that for $L/L_c < 1$, i.e., 4.5 GPa for the Hertzian pressure, the error made is less than 3%, if only one body behaves inelastically compared to two identical EP bodies in contact. It should be also noticed that, if two different elastic-plastic hardening laws are considered for the bodies in contact, the difference between the E_EP and EP_EP solutions will be lowered, making more appropriate the simplification of considering the harder material as purely elastic.

4 Modeling of the Rolling/Sliding Contact Between Two (Thermal)-Elastic-Plastic Asperities Using the dd Formulation

In the current incremental procedure, the normal contact is solved at every step. The geometry, the hardening state as well as the plastic strains are updated at the end of each step for each EP body. When the asperities are moving the geometry change includes the permanent deformation of the surface of the elastic-plastic bodies. Special care to the effects of sliding is given since it is a more complex problem than the pure rolling situation as discussed earlier.

The analysis of the contact between two asperities requires considering a relative velocity between the bearing surfaces. In addition when the tugging asperities bear only a small portion of the total load, it is clear that this transient contact will be better described by the dd formulation than by the ld one since both the subsequent localized normal and tangential loads will quickly change from zero to a maximum and then go back to zero (meaning no contact). A schematic view at the beginning of the collision is shown in Fig. 9 when one of the asperities is being translated along the rolling/sliding direction relatively to the other one. For simplicity it is assumed that the center of the two colliding asperities in Fig. 9 remains in the plane (XZ).

4.1 Update of the Geometry, Hardening, and Plastic Strains. The first step in transient contact calculation is to compute the static normal contact. If one of the bodies is considered elastic, then at the end of the first contact calculation, one has the situation presented on the left-hand side in Fig. 10(a). For the next step, the residual displacement, the hardening state and the plastic

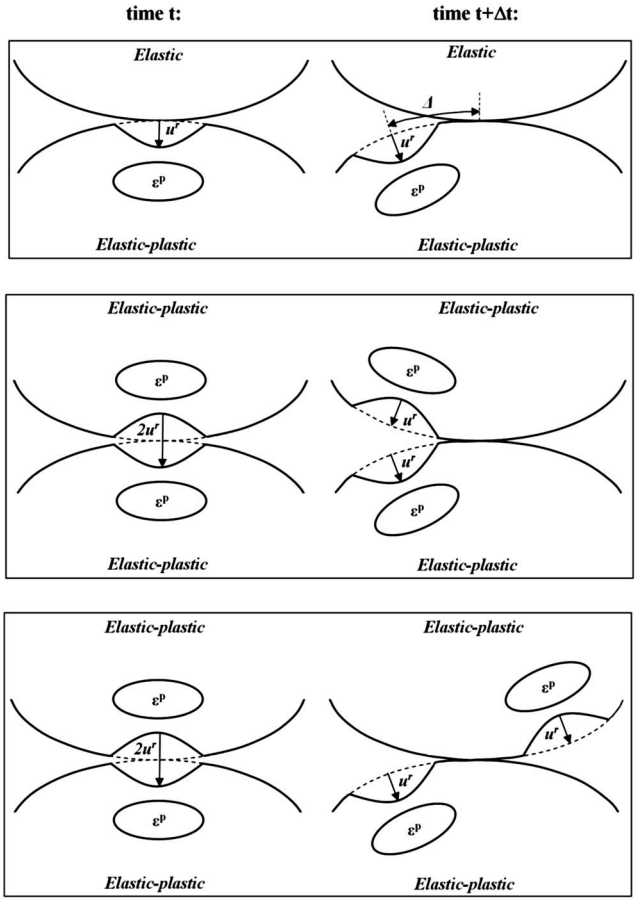

Fig. 10 Updating at the end of the first loading step. (*a*) One of the bodies is elastic. (*b*) Both bodies are elastic-plastic. Case of pure rolling. (*c*) Both bodies are elastic-plastic. Case of rolling plus sliding contact.

strains are simply shifted from a value noted Δ and the new contact calculation can be processed, see right hand side in Fig. 10(a). As a general comment, this "updating" is only possible with the assumption that both bodies are considered as half-spaces, to be coherent with the SAM used and its limitations (see [7,8]).

If both bodies are considered elastic-plastic, the pure rolling and the rolling plus sliding situations should be differentiated. For the pure rolling case, starting from the initial configuration given on the left hand side in Fig. 10(b), the problem is very similar to the contact between an elastic body pressed against an elastic-plastic body, except that (i) the hardening state and the plastic strains are simply shifted for both bodies after each step; (ii) whereas the residual displacement is doubled, as seen on the right hand side in Fig. 10(b). The new contact calculation can then be processed.

For the (rolling plus) sliding contact the situation is more complicated. Starting from the initial configuration described on the left-hand side in Fig. 10(c), where the hardening state and the plastic strains are simply shifted, it is clear that the residual displacement history should be considered individually for each surface, as it can be seen on the right-hand side in Fig. 10(c).

4.2 Calculation of the Local Interference. A global and a local reference will be considered to model the transient contact during tugging, as shown Fig. 9. The local reference (x', z') is linked to the plane of contact. A global interference is first applied in the global reference, by maintaining the global center separation, ω, along the Z direction constant during tugging. Then one of the bodies is shifted of d in the perpendicular direction (X direc-

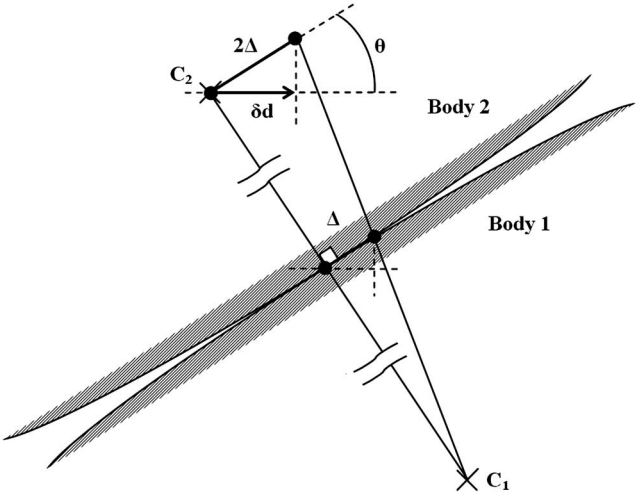

Fig. 11 Displacement δd of body 2

tion). As a consequence, the local center separation, ω', along the z' direction of the local reference will be different at every step of the computation.

The initial state is considered first, see Fig. 9. The global center separation ω is applied in the Z direction, and the two bodies are put in contact. If d_0 is the initial distance between the two centers C_1 and C_2 in the X direction, then the local center separation ω' in the z' direction can be expressed as a function of the global center separation ω, d_0 and d, the latter being the sliding distance in X direction (see Eq. (26)) and d_0 the distance defined by Eq. (27). In the whole development, both radii R_1 and R_2 are equal to R_0.

$$\omega'^2 = \omega^2 + (d_0 - d)^2 \tag{26}$$

$$\text{with} \quad d_0^2 = (R_1 + R_2)^2 - \omega^2 = 2R_0^2 - \omega^2 \tag{27}$$

In this formulation, the fixed value is the shifting value Δ introduced in Fig. 10(a). As a consequence, it is required to express the sliding distance d as a function of Δ. At any time, if one of the bodies is displaced from a value δd, its surface makes an angle θ with the shifting direction (see Fig. 11). It is then possible to write

$$\delta d = 2\Delta \cos\theta \tag{28}$$

Considering the curvature of the bodies, a correction has to be made to the value δd. Denoting $\hat{\Delta}$ the real shifted value (see Fig. 12), and writing that

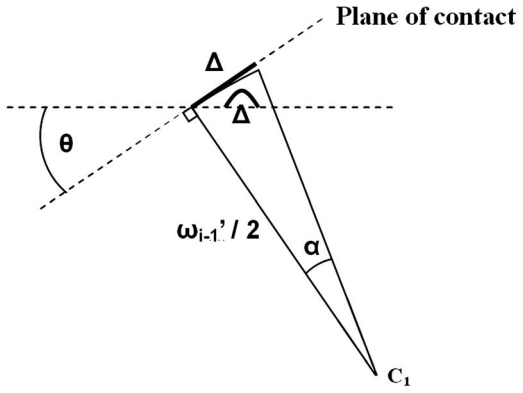

Fig. 12 Correction of the term δd

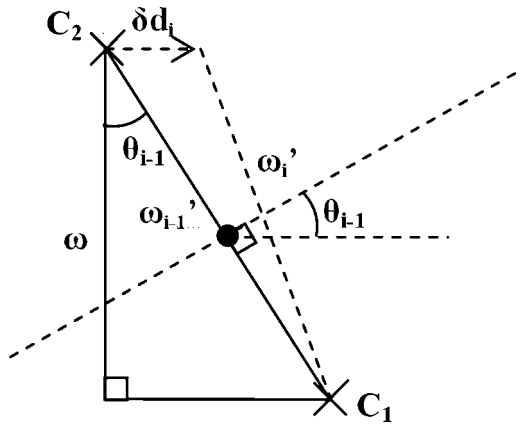

Fig. 13 Representation of two consecutive states $i-1$ and i for the determination of θ_{i-1}

$$\tan\alpha = \frac{\Delta}{\omega'_{i-1}/2} \tag{29}$$

ω'_{i-1} being the previous local center separation, δd can be corrected as follows

$$\delta d = 2\hat{\Delta}\cos\theta \tag{30}$$

$$\text{with} \quad \hat{\Delta} = (\omega'_{i-1}/2)\alpha = (\omega'_{i-1}/2)\tan^{-1}\left(\frac{\Delta}{\omega'_{i-1}/2}\right) \tag{31}$$

Then δd can be re-written as follows

$$\delta d_{i-1} = \omega'_{i-1}\tan^{-1}\left(\frac{\Delta}{\omega'_{i-1}/2}\right)\cos\theta_{i-1} \tag{32}$$

Now θ is determined, which is an unknown and varies with the sliding distance. Considering two consecutive states $i-1$ and i (see Fig. 13), one can write

$$\cos\theta_{i-1} = \frac{\omega}{\omega'_{i-1}} \tag{33}$$

Coupling Eqs. (32) and (33), it yields

$$\delta d_i = \omega\tan^{-1}\left(\frac{2\Delta}{\omega'_{i-1}}\right) \tag{34}$$

The last step in the determination of the sliding distance d is the summation of all the sliding distance increments, i.e.

$$d_i = \sum_{k=1}^{i}\delta d_k \tag{35}$$

i being the current state. The explicit form of d_i is then

$$d_i = \omega\sum_{k=0}^{i-1}\tan^{-1}\left(\frac{2\Delta}{\omega'_k}\right) \tag{36}$$

Finally, combining Eqs. (26), (27), and (36), the local center separation can be re-written as follows, at every step of the computation

$$\omega'_0 = (R_1 + R_2) = 2R_0 \tag{37}$$

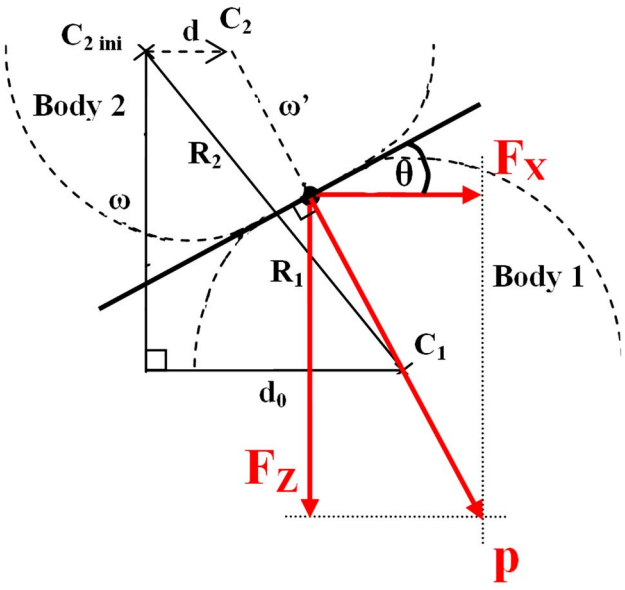

Fig. 14 Projection in the global reference of the force at a point of the contact surface

$$i > 0: \quad \omega_i' = \left\{ \omega^2 + \left[(2R_0^2 - \omega^2)^{1/2} - \omega \sum_{k=0}^{i-1} \tan^{-1}\left(\frac{2\Delta}{\omega_k'}\right) \right]^2 \right\}^{1/2} \tag{38}$$

In order to relate the local center separation ω' to the interference (rigid body approach) α used in the semi-analytical code developed previously, one can write

$$\alpha_i = 2R_0 - \omega_i' \tag{39}$$

4.3 Force Calculation and Results. The first part of this section deals with the force calculation that is projected in the global reference. Some correction term will be added in order to take into consideration what the authors refer as "pile-up" phenomenon. Finally, some results will be plotted concerning the tangential and normal forces found during the sliding phase, as well as the energy loss in the sliding contact, and the residual deformation after unloading at the end of the sliding process.

Force Calculation in the Global Reference. At any time during sliding, it is possible to calculate the pressure distribution resulting from the normal contact in the local reference. As a consequence, the tangential and the normal forces in the global reference can be calculated by integrating the pressures on the X and Y axes for the tangential forces, and on the Z-axis for the normal force, i.e.

$$F_X = na_x a_y \sum_{I_c} p \sin\theta \tag{40}$$

$$F_Y = 0 \tag{41}$$

$$F_Z = na_x a_y \sum_{I_c} p \cos\theta \tag{42}$$

n being the number of nodes where the contact pressure is not nil, a_x and a_y the grid spacings in x' and y' directions, respectively (local reference), and I_c the set of nodes where the pressure is not nil. As an example, Fig. 14 shows how to obtain the projected forces at a point of the contact surface. Due to the symmetry of the problem, the projected force F_Y on the Y axis is nil.

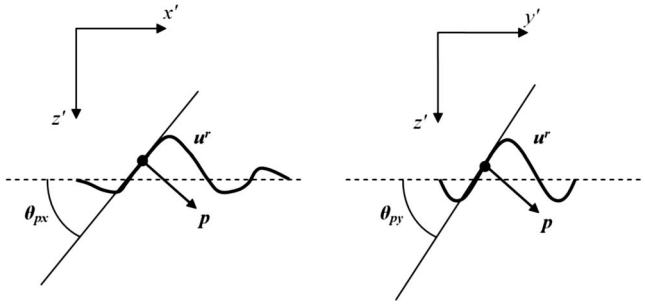

Fig. 15 Effect of the pile-up due to the slope of the residual displacement

Correction Term Induced by the "Pile-Up". The previous force calculation only takes into account the macro-scale projection. In order to include the effect of the pile-up, it is necessary to study the micro-scale projection. Figure 15 shows a magnified view at the point where the pressure p is applied. The residual displacement u^r has a slope that makes an angle θ_{px} with the x' axis and θ_{py} with the y' axis. From this observation, Eqs. (40)–(42) can be corrected as follows

$$F_X = na_x a_y \sum_{I_c} p \sin(\theta - \theta_{px}) \tag{43}$$

$$F_Y = na_x a_y \sum_{I_c} p \sin(-\theta_{py}) \tag{44}$$

$$F_Z = na_x a_y \sum_{I_c} p \cos(\theta - \theta_{px})\cos(\theta_{py}) \tag{45}$$

$$\text{with} \quad \theta_{px} = \tan^{-1}\left(\frac{\partial u^r}{\partial x}\right) \tag{46}$$

$$\text{and} \quad \theta_{py} = \tan^{-1}\left(\frac{\partial u^r}{\partial y}\right) \tag{47}$$

From Eq. (33), θ can be expressed as

$$\theta = \cos^{-1}\left(\frac{\omega}{\omega_i'}\right)\text{sign}(\omega_i' - \omega_{i-1}') \tag{48}$$

Results. The next simulations have been inspired from the work of Vijaywargiya and Green [18], who modeled the sliding contact between two cylinders using a finite element model. For the current simulations, two spherical asperities will interact. The radius of the spheres can be taken arbitrarily, so $R_1 = R_2 = 1$ m has been chosen. The elastic properties are $E_1 = E_2 = 200$ GPa for the young moduli, and $\nu_1 = \nu_2 = 0.32$ for the Poisson ratios. The chosen hardening law holds for perfect plasticity with parameter $S_y = 0.9115$ GPa for the yield stress.

In most of the results presented, values are normalized by the critical values defined by Green in [26] corresponding to the onset of yielding when plasticity just starts occurring

$$\alpha_c = \left(\frac{\pi C S_y}{2E'}\right)^2 R \tag{49}$$

$$P_c = \frac{(\pi C S_y)^3 R^2}{6E'^2} \tag{50}$$

$$U_c = \frac{(\pi C S_y)^5 R^3}{60E'^4} \tag{51}$$

with α_c the critical interference, P_c the critical load, and U_c the maximum potential energy stored during elastic deformation that

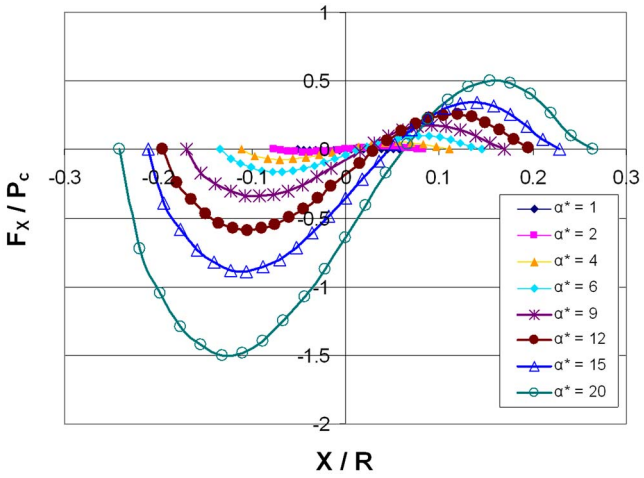

Fig. 16 Dimensionless tangential force during sliding versus dimensionless sliding direction

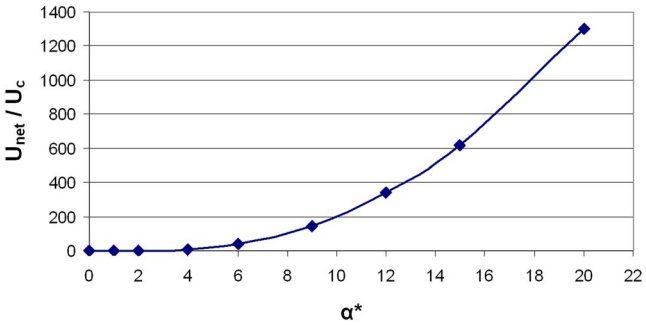

Fig. 18 Dimensionless net energy versus dimensionless interference

is equal to the work done. In these equations, parameter C is expressed in function of Poisson ratio [26]

$$C(\nu) = 1.30075 + 0.87825\nu + 0.54373\nu^2 \qquad (52)$$

Hereafter are plotted the reaction forces during the first sliding pass. The forces are normalized by the critical force found in Eq. (50), here, $P_c = 3.461 \times 10^5$ N, and the abscissa along the sliding direction by the equivalent radius; i.e. $R = 0.5$ m. Figures 16 and 17 give the tangential and the normal forces, respectively, when increasing the dimensionless interference α^*; i.e., the interference found in Eq. (39) normalized by the critical interference found in Eq. (49). It can be seen in Fig. 16 that for small interference values, the tangential force is anti-symmetric, and vanishes when the asperities are perfectly aligned; i.e., for $X/R = 0$. On the other hand, for large values of the interference, one can see that the curve is not antisymmetric anymore. This means that most of the energy (area under the curve) is produced during loading, i.e., before the asperities are aligned, and just a small part of the energy is released during unloading, i.e., when the asperities are repulsing each other. In addition the value of the force when the asperities are aligned no longer vanishes; this phenomenon is due to plastic deformation. Indeed, the residual displacement on the surface of the bodies induces some pile-up since the normal contact plane is not parallel to the sliding direction any longer. The normal force plotted in Fig. 17 is symmetric for low interference values. A slight asymmetry then begins to appear when increasing the interference; however, it is less pronounced than for the tangential force. Again, this phenomenon is due to plasticity, since due to the permanent deformation of the surface that takes place during the first loading cycle, the normal contact plane and the sliding direction are not parallel.

To give an idea of energy loss during the sliding process, Fig. 18 shows the evolution of the net energy normalized by the critical energy found in Eq. (51), versus the dimensionless interference.

A load ratio is now defined as F_X/F_Z the ratio of the tangential force over the normal one. Results are plotted in Fig. 19 versus the normalized sliding distance. It should be noted that the current simulation was made under the assumption of frictionless contact; therefore, the load ratio is only related here to the ploughing or tugging phenomena. It can be seen that for small interference values this ratio is almost perfectly antisymmetric. An increase of the load ratio is found at the beginning of the tugging (left part of Fig. 19) when increasing the interference. Conversely the F_X/F_Z ratio tends to reach an asymptotic value of 0.045 at the end of the contact (right part of the curves). In addition, it can be observed that this ratio is no longer nil when the asperities are aligned, this offset increasing with the interference value. It is again assumed to be due to plastic deformation inducing pile-up.

Another interesting result is the evolution of the permanent deformation of the surface. Figure 20 shows the maximum value of the residual displacement after unloading normalized by the critical interference given in Eq. (49), as a function of the interference. It shows a very significant residual deformation of the surface, up to 25% of the interference.

Representative computation times corresponding to $\alpha^* = 9$, for the mesh-size $dx = 3.85$ mm, $dy = 7.7$ mm, $dz = 1.925$ mm (i.e.,

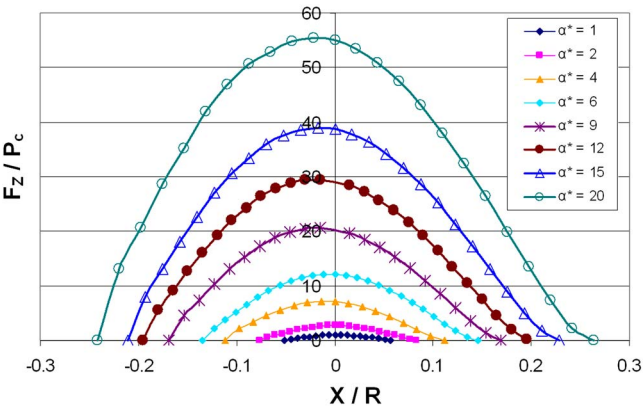

Fig. 17 Dimensionless normal force during sliding versus dimensionless sliding direction

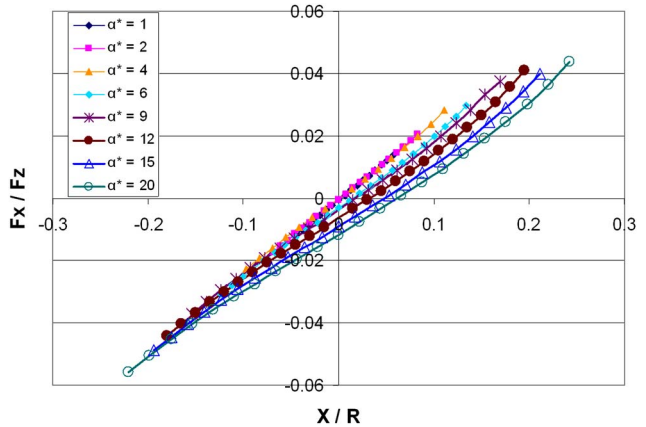

Fig. 19 Load ratio during sliding versus dimensionless sliding direction

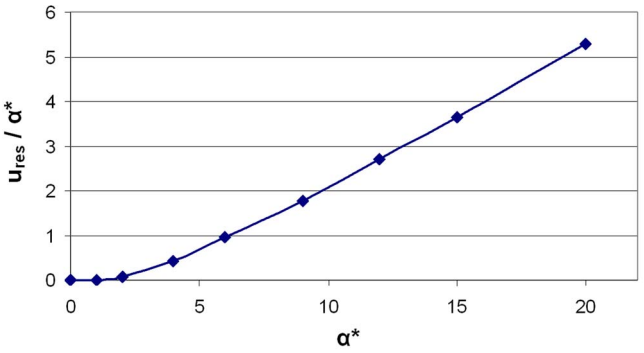

Fig. 20 Dimensionless residual displacement versus dimensionless interference

$33 \times 13 \times 31 = 13{,}299$ points), in the plastic zone and 25 time-step increments to describe the relative motion, took about 25 min on a 1.8 GHz Pentium® M personal computer.

5 Conclusion

For modeling an elastic-plastic rolling/sliding contact, a tridimensional elastic-plastic code has been adapted, requiring some specific developments. A new formulation has been proposed to drive the computation by imposing a normal rigid body displacement also called contact interference. Thanks to the use of optimized numerical techniques, which are the conjugate gradient and the discrete convolution and fast fourier transform, the computation time remains very reasonable in comparison to similar but 2D only analysis performed by FEM, and despite a large number of points in the plastic zone. The contact between two identical elastic-plastic bodies has been first analyzed. A significant reduction of the contact pressure compared to the situation when a purely elastic body is in contact with an elastic-plastic one has been shown. In order to complete the study, the tugging between two single asperities has then been investigated. Results have shown that plasticity produces an asymmetry of the normal and tangential loading during the transient contact. A load ratio due to ploughing has been estimated. Compared to finite element modeling, the developed code allows the user to compute a rolling and sliding contact in very short CPU times. The current work provides the foundation to incorporate electrical-mechanical interaction between rough surfaces by progressively introducing the relevant physical phenomena.

Acknowledgment

Partial support by the Rhône-Alpes Région through an Eurodoc grant for M. V. Boucly is gratefully acknowledged.

Nomenclature

Elastic Contact Resolution (CGM)

u = normal displacement, m
p = pressure, Pa
h = surface separation, m
α = interference, m
g = gap, m
P_0 = initial load, N
P = load, N
S_g = grid area
I_g = set of nodes in the grid
I_c = set of grid nodes in contact
I_{ol} = set of grid nodes where there is no contact and where the surfaces overlap
t = direction of the gradient
r = residual
τ = step length
$A \leftarrow B$ = means that the value of B is assigned to the quantity A

(Thermal-)Elastic-Plastic Contact Resolution

u^e = elastic displacement, m
u^t = thermal displacement, m
u^r = residual displacement, m
h^0 = initial surface separation, m
ε^p = plastic strain tensor
e^p = equivalent plastic strain
$\sigma_1^r, \sigma_2^r, \sigma_3^r$ = principal components of the residual stress tensor, Pa
P^L = interpolation polynomial
P_j^L = Lagrange polynomials
$C(\%)$ = percentage difference between E_EP and EP_EP max pressures
L_c = critical load for 0.2% equivalent plastic strain, N

Elastic constants

ν = Poisson ratio
E = Young modulus, Pa
E' = equivalent Young modulus, Pa

Geometry, Sliding Contact

R_1, R_2 = radii of bodies 1 and 2, respectively, m
R = equivalent radius, m
ω = global center separation, m
ω' = local center separation, m
(X, Z) = global reference
(x', z') = local reference
d_0 = initial distance before sliding, m
d = sliding distance, m
Δ = shifting distance, m
$\tilde{\Delta}$ = corrected shifting distance, m
θ = angle of the plane of contact, rad
F_X, F_Y, F_Z = tangential loads and normal load, respectively, N
F_X/F_Z = load ratio
θ_{px}, θ_{py} = pile-up angles, rad
S_y = yield strength, Pa
α_c = critical interference, m
P_c = critical load, N
U_c = critical potential (strain) energy, N m
$C(\nu)$ = critical yield stress coefficient
U = potential (strain) energy, N m

References

[1] Polonsky, I. A., and Keer, L. M., 1999, "A Numerical Method for Solving Rough Contact Problems Based on the Multi-Level Multi-Summation and Conjugate Gradient Techniques," Wear, **231**, pp. 206–219.
[2] Lubrecht, A. A., and Ioannides, E., 1991, "A Fast Solution of the Dry Contact Problem and the Associated Sub-Surface Stress Field, Using Multilevel Techniques," ASME J. Tribol., **113**, pp. 128–133.
[3] Ju, Y., and Farris, T. N., 1996, "Spectral Analysis of Two-Dimensional Contact Problems," ASME J. Tribol., **118**, pp. 320–328.
[4] Nogi, T., and Kato, T., 1997, "Influence of a Hard Surface Layer on the Limit of Elastic Contact—Part I: Analysis Using a Real Surface Model," ASME J. Tribol., **119**, pp. 493–500.
[5] Liu, S., Wang, Q., and Liu, G., 2000, "A Versatile Method of Discrete Convolution and FFT (DC-FFT) for Contact Analyses," Wear, **243**, pp. 101–111.
[6] Liu, S., and Wang, Q., 2001, "A Three-Dimensional Thermomechanical Model of Contact between Nonconforming Rough Surfaces," ASME J. Tribol., **123**, pp. 17–26.
[7] Jacq, C., Nélias, D., Lormand, G., and Girodin, D., 2002, "Development of a Three-Dimensional Semi-Analytical Elastic-Plastic Contact Code," ASME J. Tribol., **124**, pp. 653–667.
[8] Boucly, V., Nélias, D., Liu, S., Wang, Q. J., and Keer, L. M., 2005, "Contact Analyses for Bodies with Frictional Heating and Plastic Behavior," ASME J. Tribol., **127**, pp. 355–364.
[9] Antaluca, E., Nélias, D., and Cretu, S., 2004, "A Three-Dimensional Model for Elastic-Plastic Contact With Tangential Loading—Application to a Dented

Surface," Proc. of the 2004 STLE/ASME Tribology Conference, Long Beach, California, October 24–27, 2004, Paper No. TRIB2004-64331.
[10] Jacq, C., Lormand, G., Nélias, D., Girodin, D., and Vincent, A., 2003, "On the Influence of Residual Stresses in Determining the Micro-Yield Stress Profile in a Nitrided Steel by Nano-Indentation," Mater. Sci. Eng., A, **342**, pp. 311–319.
[11] Sainsot, P., Jacq, C., and Nélias, D., 2002, "A Numerical Model for Elasto-plastic Rough Contact," Comput. Model. Eng. Sci., **3**(4), pp. 497–506.
[12] Gallego, L., Nélias, D., and Jacq, C., 2006, "A Comprehensive Method to Predict Wear and to Define the Optimum Geometry of Fretting Surfaces," ASME J. Tribol., **128**, pp. 476–485.
[13] Nélias, D., Boucly, V., and Brunet, M., 2006, "Elastic-Plastic Contact between Rough Surfaces: Proposal for a Wear or Running-in Model," ASME J. Tribol., **128**, pp. 236–244.
[14] Wang, F., and Keer, L. M., 2005, "Numerical Simulation for Three Dimensional Elastic-Plastic Contact with Hardening Behavior," ASME J. Tribol., **127**, pp. 494–502.
[15] Popescu, G., Morales-Espejel, G. E., Wemekamp, B., and Gabelli, A., 2006, "An Engineering Model for Three-Dimensional Elastic-Plastic Rolling Contact Analyses," Tribol. Trans., **49**, pp. 387–399.
[16] Popescu, G., Gabelli, A., Morales-Espejel, G. E., and Wemekamp, B., 2006, "Micro-Plastic Material Model and Residual Fields in Rolling Contact," J. ASTM Int., **3**, pp. 1–12.
[17] Chen, J., Akyuz, U., Xu, L., and Pidaparti, R. M. V., 1998, "Stress Analysis of the Human Temporomandibular Joint," Med. Eng. Phys., **20**(8), pp. 565–572.
[18] Vijaywargiya, R., and Green, I., 2006, "A Finite Element Study of the Deformation, Forces, Stress Formation, and Energy Loss in Sliding Cylindrical Contacts," *Proc. of IJTC2006, STLE-ASME Int. Joint Trib. Conf.*, San Antonio, TX, October 22–25, 2006, Preprint IJTC2006-12020.
[19] Hamilton, G. M., and Goodman, L. E., 1966, "The Stress Field Created by a Circular Sliding Contact," ASME J. Appl. Mech., **33**, pp. 371–376.
[20] Hamilton, G. M., 1983, "Explicit Equations for the Stresses beneath a Sliding Spherical Contact," Proc. Inst. Mech. Eng., Part C: Mech. Eng. Sci., **197**, pp. 53–59.
[21] Kogut, L., and Etsion, I., 2003, "A Semi-Analytical Solution for Sliding Inception of a Spherical Contact," ASME J. Tribol., **125**, pp. 99–506.
[22] Faulkner, A., and Arnell, R. D., 2000, "Development of a Finite Element Model to Simulate the Sliding Interaction Between Two, Three-Dimensional, Elastoplastic, Hemispherical Asperities," Wear, **242**, pp. 114–122.
[23] Nosonovsky, M., and Adams, G. G., 2000, "Steady-State Frictional Sliding of Two Elastic Bodies with a Wavy Contact Interface," ASME J. Tribol., **122**, pp. 490–495.
[24] Fotiu, P. A., and Nemat-Nasser, S., 1996, "A Universal Integration Algorithm for Rate-Dependent Elastoplasticity," Comput. Struct., **59**, pp. 1173–1184.
[25] El Ghazal, H., 1999, "Etude des propriétés microstructurales et mécaniques des aciers 16NiCrMo13 cémenté et 32CrMoV13 nitruré-Application à la prévision de leur limite d'endurance en fatigue de roulement," Ph.D. thesis, INSA Lyon, France.
[26] Green, I., 2005, "Poisson Ratio Effects and Critical Values in Spherical and Cylindrical Hertzian Contacts," Appl. Mech. Eng., **10**, pp. 451–462.